The Astrophysical Journal, 843:99 (9pp), 2017 July 10 https://doi.org/10.3847/1538-4357/aa7459

High-resolution Observations of the Massive Protostar in IRAS 18566+0408

P. Hofner[1,8], R. Cesaroni[2], S. Kurtz[3], V. Rosero[1,4], C. Anderson[1,4], R. S. Furuya[5], E. D. Araya[6], and S. Molinari[7]
[1] Physics Department, New Mexico Tech, 801 Leroy Place, Socorro, NM 87801, USA; phofner@nrao.edu
[2] INAF, Osservatorio Astrofisico di Arcetri, Largo E. Fermi 5, I-50125 Firenze, Italy
[3] Instituto de Radioastronomía y Astrofísica, P.O. Box 3-72 Universidad Nacional Autónoma de México, Morelia 58090, Mexico
[4] National Radio Astronomy Observatory, 1003 Lopezville Road, Socorro, NM 87801, USA
[5] Institute of Liberal Arts and Sciences, Tokushima University, 1-1 Minami Jousanjima-machi, Tokushima 770-8502, Japan
[6] Physics Department, Western Illinois University, 1 University Circle, Macomb, IL 61455, USA
[7] INAF-Istituto di Astrofisica e Planetologia Spaziale, via Fosso del Cavaliere 100, I-00133 Roma, Italy
Received 2017 March 2; revised 2017 May 8; accepted 2017 May 17; published 2017 July 10

Abstract

We report 3 mm continuum, CH_3CN(5–4) and ^{13}CS(2–1) line observations with CARMA (Combined Array for Research in Millimeter-wave Astronomy), in conjunction with 6 and 1.3 cm continuum VLA data, and 12 and 25 μm broadband data from the Subaru Telescope toward the massive proto-star IRAS 18566+0408. The VLA data resolve the ionized jet into four components aligned in the E–W direction. Radio components A, C, and D have flat centimeter SEDs indicative of optically thin emission from ionized gas, and component B has a spectral index $\alpha = 1.0$, and a decreasing size with frequency $\propto \nu^{-0.5}$. Emission from the CARMA 3 mm continuum and from the ^{13}CS(2–1) and CH_3CN(5–4) spectral lines is compact (i.e., <6700 au) and peaks near the position of the VLA centimeter source, component B. Analysis of these lines indicates hot and dense molecular gas, which is typical for HMCs. Our Subaru telescope observations detect a single compact source, coincident with radio component B, demonstrating that most of the energy in IRAS 18566+0408 originates from a region of size <2400 au. We also present UKIRT near-infrared archival data for IRAS 18566+0408, which show extended *K*-band emission along the jet direction. We detect an E–W velocity shift of about 10 km s^{-1} over the HMC in the CH_3CN lines possibly tracing the interface of the ionized jet with the surrounding core gas. Our data demonstrate the presence of an ionized jet at the base of the molecular outflow and support the hypothesis that massive protostars with O-type luminosity form with a mechanism similar to lower mass stars.

Key words: ISM: individual objects (IRAS 18566+0408, G37.55+0.20, Mol83) – stars: formation – ISM: jets and outflows

1. Introduction

The study of massive star formation throughout the Galaxy began with radio continuum surveys (e.g., Downes & Rinehart 1966), which detected many compact, thermal sources, later identified as Ultracompact H II (UCHII) regions (e.g., Harris 1973). Observations of these dense and small ionized regions culminated in several interferometric surveys (e.g., Wood & Churchwell 1989, RMS (Red MSX Source) survey by Urquhart et al. 2009, CORNISH survey by Hoare et al. 2012), where hundreds of UCHIIs were imaged at sub-arcsecond resolution. While UCHII regions are manifestations of recently formed massive stars, because of their bright radio continuum emission, it is thought that their central stars are fully formed, and located on, or near, the main sequence.

To understand how massive stars form, i.e., how they assemble most of their mass, earlier evolutionary stages must be studied. With this goal, a number of surveys were carried out during the last two decades (e.g., Molinari et al. 1996; Sridharan et al. 2002), selecting massive protostellar candidates with the criteria of dense molecular cores with large FIR luminosity, in the absence of strong radio continuum emission. A large number of such objects were cataloged and further studied in a variety of observational probes, such as masers (e.g., Hofner & Churchwell 1996; Kurtz et al. 2004; Araya et al. 2007a), highly excited molecular lines (e.g., Olmi et al. 1996; Araya et al. 2005a; Rosero et al. 2013), as well as low critical density molecular transitions to search for molecular flows (e.g., Zhang et al. 2001; Beuther et al. 2002). One particularly important result of these latter two studies was the extremely high detection rate of molecular flows toward massive protostars, which indicated that outflows are an essential ingredient in the formation of massive stars.

In this paper, we present a multi-wavelength, high angular resolution study of a massive protostellar candidate, which we have observed in the 3 mm continuum, CH_3CN(5–4) and ^{13}CS(2–1) spectral lines with CARMA (Combined Array for Research in Millimeter-wave Astronomy), and at 12 and 25 μm with the Subaru Telescope. These data are discussed in conjunction with 6 and 1.3 cm VLA continuum data (Rosero et al. 2016), as well as archival NIR data.

The high-mass protostellar candidate IRAS 18566+0408 (also known as G37.55+0.20, or Mol83) is located at a distance of 6.7 kpc, and has a reported FIR luminosity of $6 \times 10^4\ L_\odot$, equivalent to an O8 ZAMS star (Sridharan et al. 2002). The radio continuum emission at 6, 3.6, and 1.3 cm was studied by Araya et al. (2007b) at an angular scale of one arcsecond and rms noise levels of 20–100 μJy beam^{-1}. Considering the large luminosity, the centimeter continuum emission of about 0.7 mJy is much weaker than what is expected from a UCHII region and is best explained by an optically thin thermal jet oriented in the east–west direction. At 7 mm the emission is stronger and shows an elongation approximately perpendicular to the jet, which was interpreted by Araya et al. (2007b) as a circumstellar torus, possibly

[8] Adjunct Astronomer at the National Radio Astronomy Observatory, 1003 Lopezville Road, Socorro, NM 87801, USA.

containing an accretion disk at smaller scales (see their Figure 4).

IRAS 18566+0408 is associated with maser emission from the H_2O, OH, CH_3OH, and H_2CO molecules (Araya et al. 2010, and references therein, Al-Marzouk et al. 2012). Araya et al. (2010) found that the H_2CO maser undergoes periodic flares with a period of about 240 days, and the flares are correlated with similar features in the 6.7 GHz CH_3OH and 6.035 GHz OH masers (Al-Marzouk et al. 2012). A possible explanation for this behavior is maser gain changes due to the infrared radiation of periodic accretion from a binary within a circumbinary disk (Araya et al. 2010; see Inayoshi et al. 2013; van der Walt 2014 for other possible models).

Zhang et al. (2007) studied IRAS 18566+0408 in several NH_3 transitions with the VLA, as well as in the SiO(2–1) and HCN (1–0) transitions with OVRO. They discovered a well collimated molecular flow centered on a compact 87 GHz continuum source, MM-1. The direction of the flow is in the SE–NW direction and approximately in the same direction as the CO-flow measured at 10″ resolution by Beuther et al. (2002). Furthermore, a strong increase of linewidth was observed at the position of MM-1, which Zhang et al. (2007) interpreted either as rotation/infall, or relative motion of unresolved protostellar cores.

In the following section, we describe our observations, and we present the data in Section 3. Section 4 contains a discussion of the obtained results. The paper concludes with a brief summary in Section 5.

2. Observations

2.1. CARMA Observation

Continuum and spectral line observations in the 3 mm window toward the IRAS 18566+0408 region were carried out with CARMA.[9] At the time of observations, CARMA was a 15 element interferometer with nine 6.1 m antennas and six 10.4 m antennas. For details of the instrument see the CARMA webpage.[10]

Data were taken in CARMA's B configuration with antenna baselines ranging from 65 to 800 m between 2008 January and February. The field of view of our observations, given by the half-power beam width of the 10.4 m antennas, was 73″, and our maps have a ∼1″ FWHM synthesized beam. The CARMA correlator recorded signals in three separate bands, each with an upper and lower sideband. Two bands were configured with a 31 MHz bandwidth (100 km s^{-1}) and 63 channels (1.6 km s^{-1} per channel), and were used to observe the ^{13}CS(2–1) ($\nu_0 = 92.494303$ GHz) and CH_3CN(5–4) ($\nu_0 = 91.971310$ GHz for $K = 3$) rotational lines in the lower sideband. One additional band was configured with 62 MHz bandwidth across 63 channels, which was also used to observe the CH_3CN (5–4) transition in the lower sideband, with a total velocity coverage of 200 km s^{-1} and a channel width of 3.2 km s^{-1}. The corresponding three bands in the upper sideband at a mean frequency of 95.9 GHz were used to detect the 3 mm continuum emission. Care was taken that the continuum bands were free of any strong line emission.

In each source-calibrator cycle, data were obtained in 10-second records with 8 minutes spent on IRAS 18566+0408 and 3 minutes on each of two calibrator sources. One of the calibrators (1751+096) was used as the gain and bandpass calibrator for IRAS 18566+0408, and the second calibrator (1827+062) was used as a test source to verify the quality of the phase transfer and other calibration steps. Radio pointing was done at the beginning of each track and every two hours thereafter. Absolute flux calibration was accomplished using the flux of 1751+096 (1.2 Jy) as determined from monitoring observations during the same time period as our target observations. Based on the repeatability of the quasar fluxes, we estimate that the random error in our source fluxes is ∼5%, and the systematic error from the planet calibration models is also on that order. We applied a line-length correction to account for changes in the delays of the optical fibers as they heat and cool during the day/night cycle. Calibration and imaging were done using the MIRIAD data reduction package (Sault et al. 1995). The rms noise in the resulting continuum map was 1 mJy beam^{-1}, and the rms noise in a channel map of the narrow and wide spectral line data was 12 and 8 mJy beam^{-1}, respectively.

2.2. VLA Observations

Observations toward IRAS 18566+0408 were carried out with the Karl G. Jansky Very Large Array (VLA)[11] at 1.3 cm in the B configuration on 2011 March 20, and at 6 cm in the A-configuration on 2011 July 27, as part of the survey reported by Rosero et al. (2016). For further details on the observations and data reduction, we refer the reader to the above paper. The VLA maps used in this work have a synthesized beam of 0.″33 × 0.″32, position angle PA = 93.°4, rms noise of 4.3 μJy beam^{-1} at 6 cm, and 0.″40 × 0.″30, position angle PA = −31.°3, rms noise is 7.0 μJy beam^{-1} at 1.3 cm.

2.3. Subaru Telescope Observations

IRAS 18566+0408 was observed with the COMICS camera on the 8.2 m Subaru Telescope on 2011 August 26, in the 12 and 25 μm continuum bands. For more details on these observations and data reduction, we refer the reader to Beltrán et al. (2014).

3. Results

3.1. VLA 6 and 1.3 cm Continuum Data

We show the VLA continuum maps in Figure 1, with the 1.3 cm emission in white contours, overlaid on the 6 cm map in color. The jet previously observed by Araya et al. (2007b) at angular resolutions of 1″–2″ is now resolved into 4 and 3 individual components at 6 cm and 1.3 cm, respectively. These components are labeled with letters A–D from east to west (Rosero et al. 2016). At the angular resolution of the VLA data, corresponding to ≈2300 au, the sources have a compact core surrounded by low level extended emission. In particular, in both wavelength bands there is an extended structure connecting the two brighter components A and B, which is

[9] Support for CARMA construction was derived from the states of California, Illinois, and Maryland, the James S. McDonnell Foundation, the Gordon and Betty Moore Foundation, the Kenneth T. and Eileen L. Norris Foundation, the University of Chicago, the Associates of the California Institute of Technology, and the National Science Foundation. Ongoing CARMA development and operations are supported by the National Science Foundation under a cooperative agreement, and by the CARMA partner universities.

[10] http://mmarray.org/

[11] The National Radio Astronomy Observatory is a facility of the National Science Foundation operated under cooperative agreement by Associated Universities, Inc.

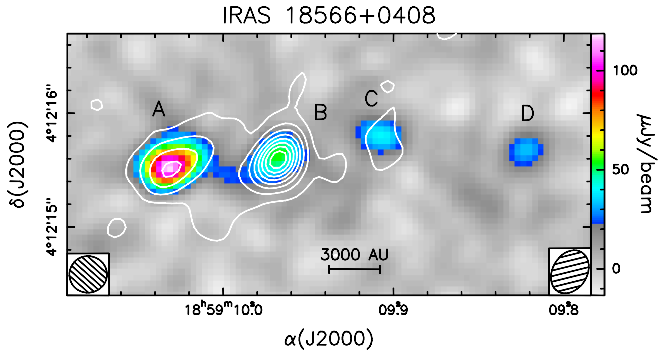

Figure 1. VLA continuum data from Rosero et al. (2016). The white contours show the combined 1.3 cm map with contour levels 24 to 192 in steps of 24 μJy beam^{-1}. The color map shows the combined 6 cm map. The synthesized beam of the 6 cm map is shown in the lower left, and that of the 1.3 cm map is shown in the lower right corner.

fairly narrow at 6 cm, but much more extended at 1.3 cm. The length of the east–west structure is about 3.″7 (25,000 au). Measured peak positions, fluxes, and peak intensities for each component are given in Table 4 of Rosero et al. (2016). If the emission is integrated over the entire structure, we find that the total flux is consistent with the lower angular resolution measurements of Araya et al. (2007b), i.e., our high-resolution maps do not miss any flux.

Rosero et al. (2016) show the spectral behavior of the continuum components in their Figure 4. Components A and C have a fairly flat spectrum, which is indicative of an optically thin thermal spectrum, and for component D a limit of $\alpha < 0.1$ is reported. Component B, on the other hand, has a distinctly different behavior. The emission strongly increases at higher frequencies and the fitted spectral index has a value of 1.0, i.e., in between the values of -0.1 for optically thin, and $+2$ for optically thick ionized gas.

A more detailed view of the run of the spectral index α can be seen in Figure 2. For this map, we have smoothed the combined 6 cm and 1.3 cm sub-band maps to the same resolution and determined α at each pixel. We also overlay on this figure a map of the average CH_3CN $J = 5$–4 $K = 0,1$ emission in contours and the positions of the 6.7 GHz CH_3OH masers from Araya et al. (2010) as filled circles. From this figure, we see that the largest spectral index occurs close to the CH_3CN maximum, which is also near the symmetry axis defined by the CH_3OH masers. The spectral index drops along the east–west jet axis, indicating also a drop in optical depth of the ionized gas.

We have fitted 2D Gaussians to the VLA continuum components A–D using the CASA task *imfit*. While components A and B are marginally resolved, components C and D are unresolved. Component B appears to be slightly extended in the east–west direction, and we find that the deconvolved source FWHM decreases as a function of frequency as $\Theta_{\rm major} \propto \nu^{\gamma}$, where $\gamma = -0.5$. This is shown in Figure 3. No variation of size as a function of frequency was detected for component A.

3.2. CARMA Data

3.2.1. 3 mm Continuum

In Figure 4(a), we show our 3.1 mm map in contours overlaid on the 6 cm radio jet in color. We measure a peak intensity of 3.8 mJy beam^{-1}, and a total flux density of

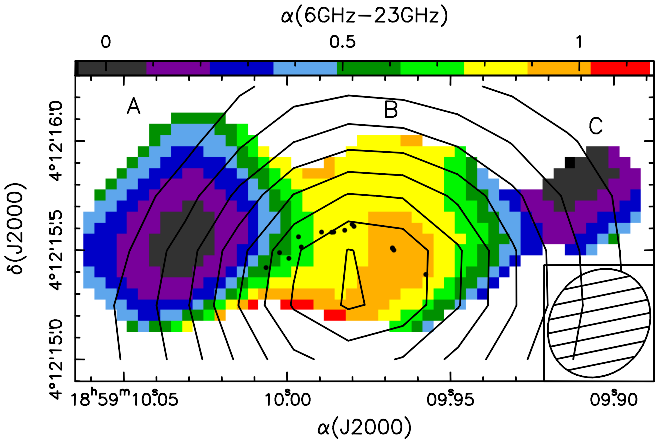

Figure 2. Map of the spectral index of the IRAS 18566+0408 jet, derived pixel-by-pixel for the combined maps at 6 and 1.3 cm . The contours show the average CH_3CN $J = 5$–4 $K = 0$, 1 emission. The black dots show the position of the CH_3OH 6.7 GHz masers from Araya et al. (2010). The beam for the centimeter data is shown in the lower right corner.

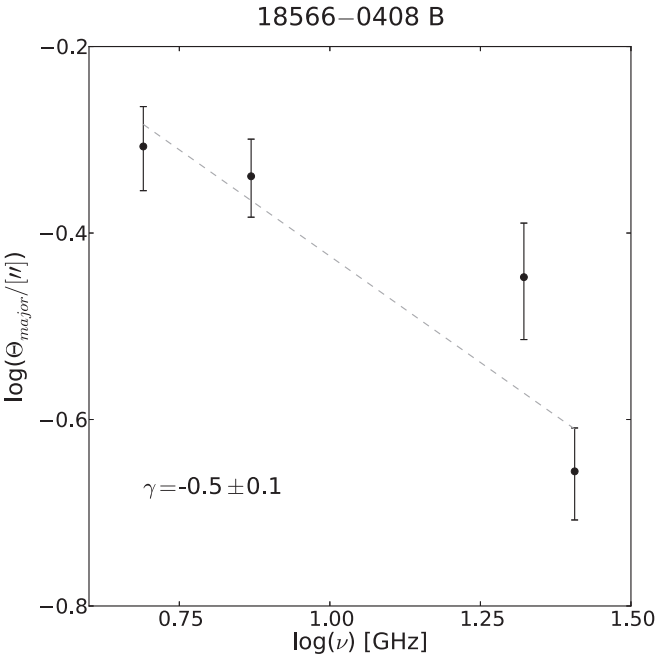

Figure 3. Deconvolved size vs. frequency relation for component B. The dashed line shows the power-law fit to the data.

7.8 mJy. The peak position of the 3.1 mm emission is at R.A. = $18^{\rm h}59^{\rm m}10.^{\rm s}01$, and decl. = $+04°12'15.''3$. In Figure 4 (a), we also show the position of the 7 mm peak position from Araya et al. (2007b), which is identical to the position of MM-1 of Zhang et al. (2007). Considering the positional accuracy of these measurements, we conclude that the millimeter emission peaks are consistent. The 3.1 mm emission in our map is slightly resolved and has a cometary shape pointing toward the east, in the direction of the jet.

Zhang et al. (2007) reported 3.4 mm observations toward this source with OVRO. Within a $\approx 5''$ beam these authors measure a peak intensity of 18 mJy beam^{-1}, and a total flux density of 31 mJy integrated over a source size of about $10''$. These data indicate an extended structure, which becomes brighter toward the center. Our observations do not have sufficient sensitivity to detect the extended emission and only trace the central core.

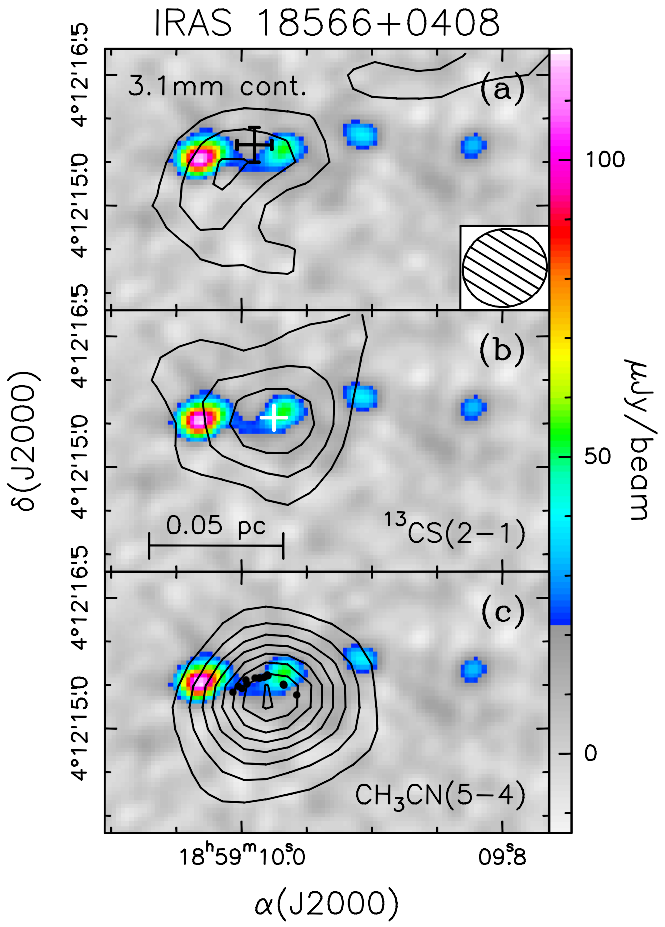

Figure 4. Contour maps of the CARMA data, with the synthesized beam size shown only in the top panel. In all images, the VLA 6 cm map is shown in color in the background. (a) Top panel: contour map of the 3.1 mm emission. Contour levels are from 1.2 to 3.6 mJy beam^{-1} in steps of 1.2 mJy beam^{-1}. The black cross marks the peak position of the 7 mm emission from Araya et al. (2007b). (b) Middle panel: contour map of the average ^{13}CS (2–1) line emission. Contour levels are from 18 to 42 mJy beam^{-1} in steps of 12 mJy beam^{-1}. The white cross marks the peak position of the 4.8 GHz H_2CO maser from Araya et al. (2005b). (c) Bottom panel: the contours show the average CH_3CN $J = 5$–4 $K = 0,1$ emission. Contour levels are from 12 to 96 mJy beam^{-1} in steps of 12 mJy beam^{-1}. The black dots show the position of the 6.7 GHz CH_3OH masers from Araya et al. (2010).

Using the formulas given in Mezger et al. (1990) with $b = 1.9$, solar metallicity, and a temperature of 80 K (Zhang et al. 2007), the 3.1 mm emission in the central synthesized beam corresponds to a total mass of about 44 $M_\odot$. This is consistent with the estimates based on the NH_3 observations of Zhang et al. (2007). These authors also reported a secondary peak, MM-2, located to the northwest of MM-1, with a peak brightness of 2.6 mJy beam^{-1} at 87 GHz. This source is not detected in our 95.9 GHz observations with a 5σ limit of 5 mJy beam^{-1}.

3.2.2. ^{13}CS(2–1)

In Figure 4(b), we show the average emission of the ^{13}CS(2–1) line in contours. The 3.1 mm continuum emission has been subtracted. The maximum of the line emission is located at R.A. = 18^{h}59^{m}09^s.98, and decl. = +04°12′15.″5, very close to the position of the H_2CO maser (Araya et al. 2005b), which is shown as a white cross. A spectrum taken at the peak pixel is shown in Figure 5. The line is fitted well by a

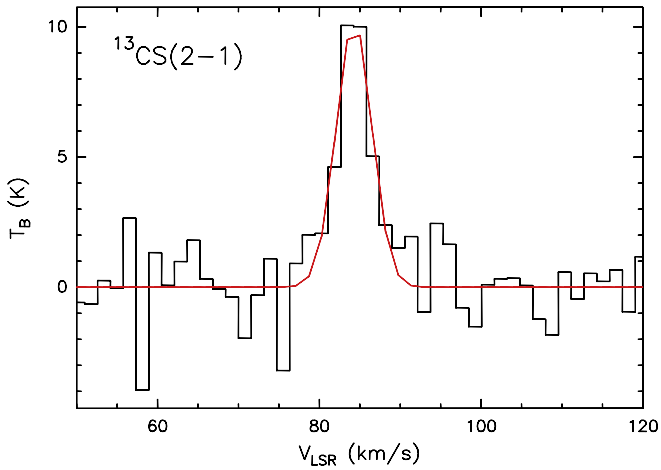

Figure 5. CARMA ^{13}CS(2–1) spectrum toward IRAS 18566+0408. The spectrum has been extracted at the peak pixel position of R.A. = 18^{h}59^{m}09^s.98 and decl. = +04°12′15.″5. The Gaussian fit is shown as the red line.

Gaussian with an integrated line flux of 57 ± 7 K km s^{-1}, a velocity of v_{LSR} = 84.3 ± 0.3 km s^{-1}, and a linewidth (FWHM) of 5.2 ± 0.8 km s^{-1}.

Using the formulas by Mehringer (1995), which assume optically thin emission under LTE conditions, and using an excitation temperature of 80 K, the integrated line flux at the peak position corresponds to a ^{13}CS column density of 1.0×10^{15} cm^{-2}. To estimate the H_2 column density one needs to know the CS abundance, as well as the ^{12}C/^{13}C isotope ratio. While the latter is fairly well known (we assume a value of 50 here), the CS abundance in hot molecular cores is highly variable due to the active chemistry in these regions. The models of Nomura & Millar (2004) predict values between 10^{-7} and 10^{-10} for the CS abundance. If we adopt a value of 10^{-8}, the hydrogen column density and total mass are consistent with what is derived from the 3.1 mm emission (see above) and implies values of $N_{H_2} = 2.1 \times 10^{24}$ cm^{-2} and $n_{H_2} = 2.3 \times 10^7$ cm^{-3} within the central 0.03 pc.

3.2.3. $CH_3CN(5–4)$

In Figure 4(c), we show the average of the CH_3CN $J = 5$–4 $K = 0, 1$ emission from the higher spectral resolution data. The black dots show the position of the CH_3OH 6.7 GHz masers from Araya et al. (2010). The CH_3CN $J = 5$–4 $K = 0,1$ emission has its peak at a position R.A. = 18^{h}59^{m}09^s.98 and decl. = +04°12′15.″3. In Figure 6, we show a spectrum of the low-resolution data taken at the peak position. We have detected all 0–4 K-components of the $J = 5$–4 transition, as well as marginal emission of the $J = 5$–4 $K = 0,1$ transition of the $CH_3^{13}CN$ isotopologue.

We fitted the expression $T_B = T_{rot}\eta(1 - e^{-\tau_\nu})$ simultaneously to all detected K-components in the following fashion. First, a Gaussian fit was carried out for the $K = 0$–4 components with the line separations fixed to their theoretical values. From this fit, we obtained the source velocity v_{LSR} = 83.9 ± 0.2 km s^{-1}. Then the expression for the brightness temperature was fit varying the four input parameters, beam filling factor η, linewidth FWHM, rotational temperature T_{rot}, and source averaged CH_3CN column density N_{CH_3CN}. The best physical fit is shown in Figure 6 as a green line. The best-fit values are $\eta = 0.17^{+0.07}_{-0.08}$, FWHM = $8.3^{+0.9}_{-0.8}$ km s^{-1}, $T_{rot} = 170^{+220}_{-60}$ K,

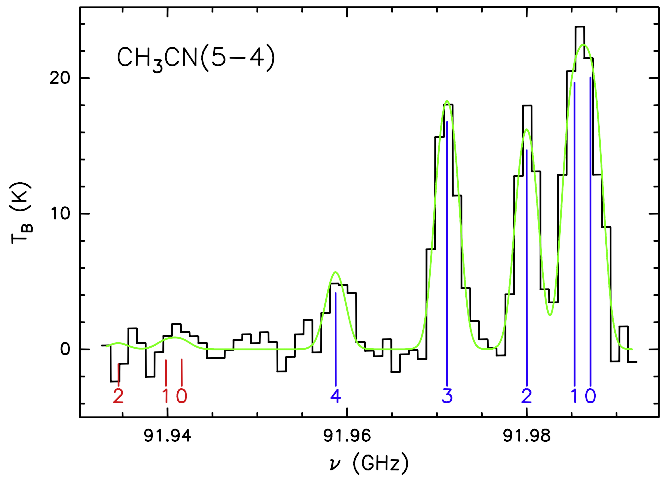

Figure 6. CARMA $CH_3CN(5–4)$ spectrum toward IRAS 18566+0408. The spectrum has been extracted at the peak pixel position of R.A. = $18^h59^m09^s.98$ and decl. = +04°12′15.″3. The green line shows the physical fit described in the text. The frequencies of the *K*-components of the $CH_3CN(5–4)$ transition are shown by blue vertical lines and those of the $CH_3^{13}CN$ isotopologue by the red line.

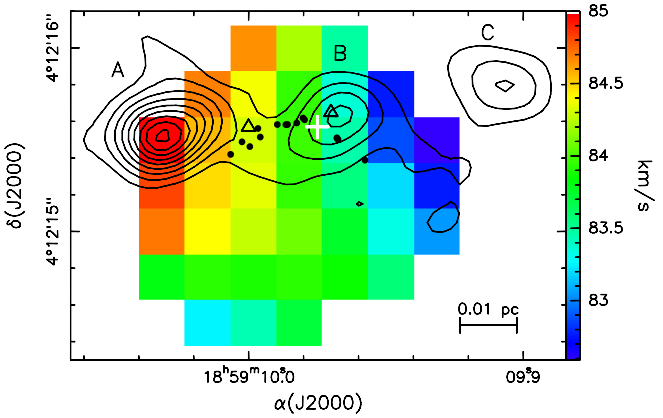

Figure 7. Velocity map of the $CH_3CN(5–4)$ $K = 0$ to $K = 3$ lines. A spectrum at each pixel was fitted with fixed linewidth and relative velocities between the *K*-components for the high spectral resolution data. An east–west velocity gradient is apparent. Overlaid are contours of the 6 cm emission, while the filled circles are the positions of the 6.7 GHz masers from Araya et al. (2010), the white cross marks the position of the H_2CO maser from Araya et al. (2005b), and the open triangles mark the position of H_2O masers (H. Beuther 2017, private communication).

and $N_{CH_3CN} = (1.1^{+9}_{-0.7}) \times 10^{17}$ cm^{-2}. The 1σ errors have been estimated using the method of Lampton et al. (1976).

Although the CH_3CN emission is only marginally resolved, we can check for velocity gradients by fitting the $CH_3CN(5–4)$ profiles (from $K = 0$ to $K = 3$) pixel-by-pixel in the map. The result of this procedure is shown in Figure 7. The typical error on the velocity is <0.4 km s^{-1}. We detect an east–west velocity gradient.

An alternative view of the velocity gradient can be obtained by fitting the peak position in each channel map and plotting the velocities versus the R.A. offsets of the corresponding peak positions. This is shown in Figure 8. A velocity shift of about 10 km s^{-1} over a distance of 0.″4 (2700 au) is detected, with redshifted velocities in the east and blueshifted velocities in the west.

3.3. Infrared Data

In the Subaru images a single point source is detected at both 12 and 25 μm, with fluxes of 11 ± 1 Jy and 80 ± 8 Jy, respectively. Since this was the only source detected in the field of view of the camera, we registered the position of this source with respect to the *SPITZER*/GLIMPSE 8 μm image. The estimated accuracy of the position of the Mid-IR source is 1.″5. The source is unresolved with the Subaru diffraction limit of 0.″36 at 12 μm, which corresponds to a linear size of 0.01 pc or 2400 au at the distance to IRAS 18566+0408 of 6.7 kpc.

We also retrieved data from the UKIRT Infrared Deep Sky Survey (UKIDSS) GPS for IRAS 18566+0408. The UKIDSS project is defined in Lawrence et al. (2007). UKIDSS uses the UKIRT Wide Field Camera (Casali et al. 2007). The photometric system is described in Hewett et al. (2006) and the calibration is described in Hodgkin et al. (2009). The pipeline processing and science archive are described in Irwin et al. (2009) and Hambly et al. (2008). The UKIDSS images are three magnitudes deeper and have higher angular resolution (~0.″4) compared to 2MASS data. The astrometric accuracy of the UKIDSS data is about 50 mas.

In Figure 9, we show an overlay of the UKIDSS *K*-band (2.2 μm) image with the VLA 6 cm contours. The position of

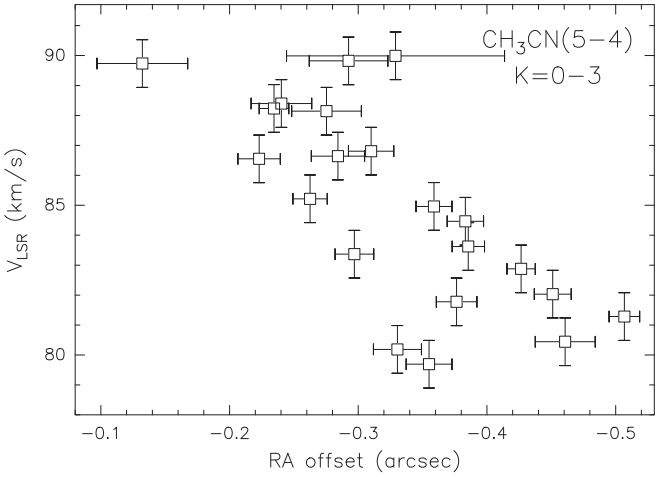

Figure 8. Plot of V_{LSR} vs. R.A. offset for the $CH_3CN(5–4)$ transition. The peak position at each velocity was obtained by fitting a 2D Gaussian to the corresponding channel map in the high spectral resolution data. Errorbars on the offsets are the formal errors from the 2D-Gaussian fit, while those on the velocities are equal to the channel width. A velocity shift of about 10 km s^{-1} over a distance of 0.″4 (2700 au) with redshifted velocities in the east and blueshifted velocities in the west is apparent.

the Mid-IR source is also shown. In the infrared *K* band there is a bright source coincident with the ionized jet. It is not detected at the infrared H or *J* band, which suggests that it is deeply embedded. The source is very extended with respect to the UKIDSS resolution and hence the most likely explanation for the *K*-band emission is scattered light.

We have also revisited the question of the total luminosity of IRAS 18566+0408. For this, we collected all available flux density measurements in the literature and plotted the spectral energy distribution in Figure 10. We obtain a value for the total luminosity of this source of $8 \times 10^4\ L_\odot$ confirming the results of Zhang et al. (2007). Inspecting the available maps in the wavelength bands between 24 μm (*SPITZER* MIPSGAL) and 500 μm (*Herschel* Hi-GAL), we found that the emission is compact and centered on the position of the massive protostellar candidate. Furthermore, there are no additional mid-IR sources within 10″ from the central source,

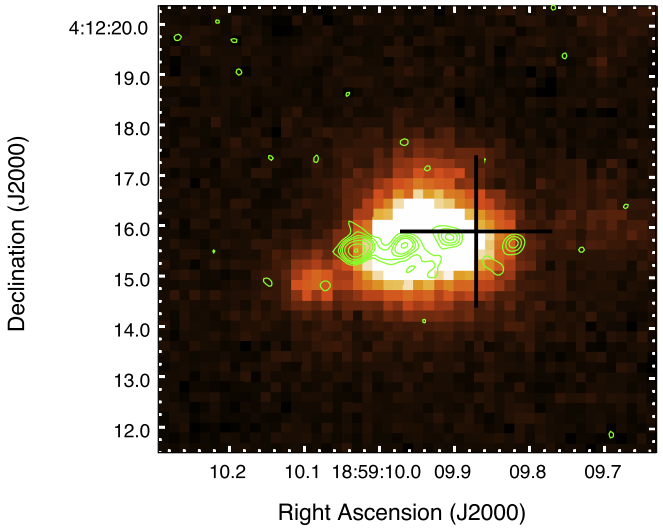

Figure 9. Infrared *K*-band (2.2 μm) UKIDSS image in color overlaid with the 6 cm contours. Contour levels are 3, 5, 7, 9, 13, 20, 29 $\times$ 4 μJy beam^{-1}. The black cross marks the position of the 25 μm emission, and the dimensions of the cross indicate its approximate astrometric accuracy.

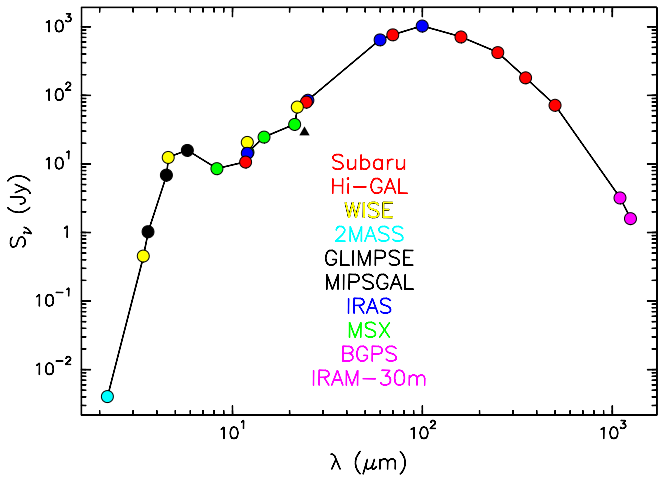

Figure 10. Spectral energy distribution toward IRAS 18566+0408. We have collected the flux densities available in the literature as shown above. The triangle marks a lower limit to the flux density due to saturation. Integrating under this curve, we obtain a value for the total luminosity of 8 $\times$ 10^4 $L_\odot$.

demonstrating that the compact mid-IR source dominates the energetics of the region.

4. Discussion

4.1. The Nature of the Centimeter Continuum Emission

Our VLA data show a linear structure oriented east–west with a length of approximately 0.1 pc, which consists of weak extended emission and four compact components. One might ask whether these sources could be explained as individual UCHII regions, and although we favor an ionized jet explanation, we will briefly comment on this hypothesis. First, calculating the required spectral types from the measured fluxes, assuming optically thin conditions, we obtain ZAMS spectral types of B2 for components A and B, and B3 for components C and D. The total luminosity of four such stars would be below 2 $\times$ 10^4 $L_\odot$, whereas the measured luminosity of IRAS 18566+0408 is 8 $\times$ 10^4 $L_\odot$; thus, the regions appear highly under-luminous. However, while absorption of UV photons by dust within the ionized gas could, in principle, explain this discrepancy (e.g., Wood & Churchwell 1989), in this case, one would expect a closer morphological correspondence in the mid-IR. As mentioned above, components A, C, and D have flat spectral indices, indicating optically thin emission, and the data are consistent with emission measures $\approx$10^5 pc cm^{-6} and electron densities of $\approx$5 $\times$ 10^3 cm^{-3}, as one would expect for small ionized regions around B2–3 type stars. For component B, the spectral index of 1.0 could be explained with a constant density H II region where the optical depth is approximately unity, i.e., between optically thick and thin emission. With this assumption, we obtain an emission measure of 2.7 $\times$ 10^9 pc cm^{-6} and a lower limit on the electron density of 5.2 $\times$ 10^5 cm^{-3}, similar to values often derived for UCHII regions (e.g., Kurtz et al. 1994). We have also calculated sizes for the hypothetical H II regions assuming that they are initial Strömgren spheres or ionized gas clouds in pressure equilibrium with the surrounding gas using the theory of Xie et al. (1996) and the data of Zhang et al. (2007). In all cases, the sources are predicted to be smaller than our resolution, in agreement with our observations. In summary then, our VLA data do not completely rule out that the four continuum sources are individual H II regions. However, due to the association with outflowing molecular gas (Beuther et al. 2002; Zhang et al. 2007), as well as shocked gas seen as *Spitzer* green-band excess (Araya et al. 2007b) in approximately the same direction, we consider an ionized jet to be a more likely explanation. Our result that component B shows a decreasing size with frequency (Figure 4) is also an expected feature of varying electron density in the source (e.g., Panagia & Felli 1975; Reynolds 1986), and hence supportive of the ionized jet assumption. We will hence adopt this hypothesis for the rest of this paper.

There are several models that can be used to calculate the expected flux from ionized jets. The work of Reynolds (1986) predicts the centimeter emission from partly ionized collimated winds without specifying the source of ionization, and the work of Curiel et al. (1987, 1989) discusses the case of cm emission from an ionized plasma where a neutral wind shocks molecular matter surrounding the protostar. Most researchers have favored the model of Curiel et al. (1989) to explain observed jet sources (e.g., Hofner et al. 2007; Johnston et al. 2013). Both models depend on many physical parameters, which are generally not known, but adopting a number of assumptions we can obtain estimates for the mass loss ($\dot{M}$) and momentum rate ($\dot{P}$) for the jets. Thus, adopting the usual set of assumptions (e.g., Rosero et al. 2014), we can apply equation (19) of Reynolds (1986) to our radio component B, to estimate a mass-loss rate of $\dot{M} = 1.1 \times 10^{-5}\,M_\odot$ yr^{-1}, and a momentum rate of $\dot{P} = 7.7 \times 10^{-3}\,M_\odot$ yr^{-1} km s^{-1}. It is interesting to note that Beuther et al. (2002) obtain a similar number for $\dot{P}$, based on their IRAM 30 m CO(2–1) maps, which would indicate sufficient force in the jet to drive the larger scale molecular flow.

For the case of shock ionization, Anglada et al. (1992) has shown that for low-mass objects the relation between momentum rate and centimeter luminosity follows a power law described by $\dot{P} = 10^{-2.6}(S_\nu d^2)^{1.1}$ (where $\dot{P}$ is in units of $M_\odot$ yr^{-1} km s^{-1}, and $S_\nu d^2$ in units of mJy kpc^2), and Rodriguez et al. (2008) have shown that three high luminosity objects with ionized jets also follow this relationship. For component B at

7.4 GHz we have a centimeter luminosity of 2.8 mJy kpc^2, which results in a predicted momentum rate of $\dot{P} = 8.0 \times 10^{-3}\,M_\odot\,\mathrm{yr}^{-1}\,\mathrm{km\,s}^{-1}$, i.e., virtually identical to the value measured by Beuther et al. (2002), and what is implied by the formula of Reynolds (1986). We hence add an additional data point to the $\dot{P}$ versus $S_\nu d^2$ relation, which further strengthens the hypothesis that the ionized jets observed from massive young objects are operating with the same physical mechanism as those from low-mass stars.

4.2. The Nature of the CH_3CN Velocity Gradient

The molecular line data observed with CARMA allow an interesting view on the kinematics in the IRAS 18566+0408 core. Zhang et al. (2007) detected an increase of FWHM in the NH_3 lines from 5.5 km s^{-1} at an angular resolution of 3″, to 8.7 km s^{-1} at an angular resolution of 1″. They discuss this increase of linewidth in terms of outflow, infall, rotation, or relative motion of multiple objects in the synthesized beam. These authors also mapped a collimated flow in the SiO(2–1) line centered on the millimeter peak position, which is oriented in the SE–NW direction, with blueshifted emission extended mostly toward the NW, and a smaller emission region at redshifted velocities toward the SE. A similarly oriented flow was also observed by Beuther et al. (2002) in the CO(2–1) line with the IRAM 30 m telescope.

We have detected a change of velocity in the CH_3CN lines along the jet of about 10 km s^{-1} along the east–west direction. This confirms the broadening of the spectral lines toward smaller scales observed by Zhang et al. (2007). The alignment of the velocity gradient with the ionized jet strongly suggests that the gas traced by the CH_3CN(5–4) line represents outflowing matter at the base of the flow. We note that the CH_3OH and H_2O masers are also distributed along an east–west direction, with a velocity gradient consistent with that of CH_3CN. Since the CH_3CN emission is only marginally resolved at an angular scale of 1″, and our fitting technique is essentially sub-resolution, the outflowing gas is mostly arising from distances <6700 au from the massive protostar. Our line fitting results indicate a low beam filling factor of $\eta = 0.17^{+0.07}_{-0.08}$, suggesting that most of the emission occurs on scales of ≈0.″5. We have derived temperatures and column densities of $T_{\rm rot} = 170^{+220}_{-60}$ K and $N_{\rm CH_3CN} = (1.1^{+9}_{-0.7}) \times 10^{17}$ cm^{-2}. We compare these values with the results, which were recently reported by Hernández-Hernández et al. (2014) based on lower resolution SMA CH_3CN(12–11) data of this region. These authors used a two component model consisting of a lower density cooler region, plus a compact higher density and hotter region to fit their spatially unresolved spectrum. Due to the relatively large error in our temperature determination, our value for the temperature is consistent with either of these components. Our relatively high column density is also consistent with what Hernández-Hernández et al. (2014) derive from fitting their compact component if we account for the difference in assumed size for the emitting region. As discussed in Comito et al. (2005), the χ^2 fits to the spectrum are generally not unique, hence we caution the reader that the size of the emitting region remains uncertain. Higher angular resolution observations, which fully resolve the CH_3CN emission will be necessary to clarify this point.

Adopting then for the remainder of this discussion the physical values derived in our analysis, we can ask what the likely astrophysical scenario responsible for the CH_3CN emission is. The detected E–W velocity gradient, and the spatial coincidence with the jet, suggests that the CH_3CN emission traces an outflow associated with the ionized jet very near the central protostar. As discussed above, the momentum rate of the ionized jet appears sufficient to drive the large-scale molecular flow. One possible interpretation of the velocity gradient of the CH_3CN lines is that we have detected the high pressure neutral gas adjacent to the jet, i.e., the region where the jet imparts momentum and accelerates the molecular gas. Two physical mechanisms for momentum transport have been discussed in the literature: the formation of a turbulent mixing layer via the Kelvin–Helmholtz instability, or alternatively via bow shocks (e.g., Cantó & Raga 1991; Chernin et al. 1994). Most jets from young stellar objects are highly supersonic (e.g., Guzmán et al. 2016) and in this case momentum transfer via bow shocks is predicted to dominate (Chernin et al. 1994). Since the IRAS 18566+0408 jet appears to lie very close to the plane of the sky, the detected velocity shift along the jet axis of about 10 km s^{-1} indicates that the 3D space velocities are much higher, and also highly supersonic. We note that while the emission in the CH_3CN lines has often been assigned to a rotating disk perpendicular to the outflowing gas (e.g., Cesaroni et al. 2014), CH_3CN emission has also been reported as a tracer of outflows (Leurini et al. 2011 in IRAS 17233-3606, Palau et al. 2017 in IRAS 20126+4104) and of bow shocks (Codella et al. 2009 for L1157-B1).

Our data allow us to compare the thermal pressure of the ionized jet near its base with the thermal pressure of the surrounding molecular gas, to investigate whether the molecular gas will inhibit the sideways expansion of the jet and contribute to its collimation. The ionized gas has a lower limit on the electron density of 5.2×10^5 cm^{-3} (see above) and assuming an electron temperature of 10^4 K, we have $P/k \geqslant 5 \times 10^9$ K cm^{-3} (where k is the Boltzmann constant). To estimate the pressure in the surrounding molecular gas, we need to assume an abundance for CH_3CN relative to H_2, which can vary between 10^{-7} and 10^{-10} in chemically active hot core regions (e.g., Nomura & Millar 2004; Calcutt et al. 2014). Using a common assumption for the abundance ratio of 10^{-8} and a temperature of 170 K, the resulting thermal pressure is $P/k \approx 7 \times 10^8$ K cm^{-3}, which is an order of magnitude lower than the limit on the thermal pressure in the jet. It is thus likely that the neutral gas will not inhibit sideways expansion of the jet material, and a different collimation mechanism is needed.

4.3. Comparison with IRAS 16562−3959

Finally, it is interesting to compare IRAS 18566+0408 with a source which, while located at a much closer distance of 1.7 kpc, appears strikingly similar, namely the jet source IRAS 16562−3959. While many studies of protostars with bolometric luminosities corresponding to early B-type stars exist, these two sources are rare examples of massive protostars with an O-type luminosity. Both sources have a linear string of radio sources that are best interpreted as ionized gas due to shocks from fast jets. IRAS 16562−3959 shows radio lobes at distances out to 0.4 pc from the central object, and both sources have inner radio lobes at distances of the order of 10,000 au. In the case of IRAS 16562−3959, the proper motion of the radio lobes with approximately 500 km s^{-1} was recently measured by Guzmán et al. (2016),

proving without doubt their jet origin. For both sources, the radio spectra for the lobes are flat whereas the central object has a rising spectral index of about 1. Also, for both sources, the central source shows a decreasing size with frequency, which is suggestive of an ionized jet. However, based on RRL data, Guzmán et al. (2014) model the radio emission from the central source in IRAS 16562−3959 as an HCHII region with a slow ionized wind. Clearly, both sources are very rare examples of massive protostars that are still in an accretion phase during their formation. One might speculate that IRAS 18566+0408 is perhaps in a somewhat earlier evolutionary state due to its more compact nature, high level of maser emission, and due to the presence of high pressure molecular gas at the base of the jet. The presence of jets in both sources strongly supports the hypothesis that the disk accretion model also applies to massive protostars with O-type luminosity.

5. Summary

In this paper, we presented high angular resolution observations at centimeter, millimeter, and mid-IR wavelengths toward the massive protostellar candidate IRAS 18566+0408. The main results are as follows.

(1) Our VLA data in the 6 and 1.3 cm wavelength band resolve the ionized jet into four components. These are aligned in the E–W direction consistent with other outflow tracers in this source. Radio components A, C, and D have flat centimeter SEDs indicative of optically thin emission from ionized gas, and component B has a spectral index $\alpha = 1.0$, and shows a decreasing size with frequency with $\gamma = -0.5$ as expected from an ionized jet.
(2) We have detected compact (i.e., <6700 au) emission in the 3 mm continuum, and in the ^{13}CS(2–1), and CH_3CN(5–4) spectral lines, which peak near the position of continuum component B. Physical analysis of these lines indicates hot and dense molecular gas with values typical for HMCs.
(3) Our Subaru telescope observations detect a single compact source at 12 and 25 μm, which is coincident with radio component B. This demonstrates that most of the luminosity in IRAS 18566+0408 originates from a region of size <2400 au.
(4) We also present UKIRT near-infrared archival data for IRAS 18566+0408. The source is only detected at the infrared K band, and the extended nature of the emission elongated along the jet direction, most likely indicates scattered light.
(5) We detect an E–W velocity shift of about 10 km s^{-1} over the HMC in the CH_3CN lines. It is possible that the dense and hot molecular gas traces the interface of the ionized jet with the surrounding molecular core gas. If the CH_3CN abundance is assumed to have the typical HMC value of 10^{-8}, the thermal pressure in the ionized jet exceeds the thermal pressure in the molecular gas, and the sideways expansion of the ionized gas is not sufficiently inhibited, hence an additional collimation mechanism may be needed.

P.H. acknowledges support from NSF grant AST-0908901 for this work. Support for this work was provided by the NSF through the Grote Reber Fellowship Program administered by Associated Universities, Inc./National Radio Astronomy Observatory (CA and VR). We thank S. Schnee for help with CARMA data reduction. Some of the data reported here were obtained as part of the UKIRT Service Program. The United Kingdom Infrared Telescope is operated by the Joint Astronomy Centre on behalf of the UK Particle Physics and Astronomy Research Council. We thank H. Beuther for providing accurate H_2O maser positions. Further thanks are due to the anonymous referee, whose comments improved this manuscript.

References

Al-Marzouk, A. A., Araya, E., Hofner, P., et al. 2012, ApJ, 750, 170
Anglada, G., Rodriguez, L. F., Cantó, J., Estalella, R., & Torrellles, J. M. 1992, ApJ, 395, 494
Araya, E., Hofner, P., Goss, W. M., et al. 2007a, ApJS, 170, 152
Araya, E., Hofner, P., Goss, W. M., et al. 2010, ApJL, 717, L133
Araya, E., Hofner, P., Kurtz, S., Bronfman, L., & DeDeo, S. 2005a, ApJS, 157, 279
Araya, E., Hofner, P., Kurtz, S., et al. 2005b, ApJ, 618, 339
Araya, E., Hofner, P., Sewilo, M., et al. 2007b, ApJ, 669, 1050
Beltrán, M. T., Sánchez-Monge, Á., Cesaroni, R., et al. 2014, A&A, 571, 52
Beuther, H., Schilke, P., Sridharan, T. K., et al. 2002, A&A, 383, 892
Calcutt, H., Viti, S., Codella, C., et al. 2014, MNRAS, 443, 3157
Cantó, J., & Raga, A. C. 1991, ApJ, 372, 646
Casali, M., Adamson, A., Alves de Oliveira, C., et al. 2007, A&A, 467 777
Cesaroni, R., Galli, D., Neri, R., & Walmsley, C. M. 2014, A&A, 566, 73
Chernin, L., Masson, C., Gouveia dal Pino, E. M., & Benz, W. 1994, ApJ, 426, 204
Codella, C., Benedettini, M., Beltrán, M. T., et al. 2009, A&A, 507, L25
Comito, C., Schilke, P., Phillips, T. G., et al. 2005, ApJS, 156, 127
Curiel, S., Cantó, J., & Rodriguez, L. F. 1987, RMxAA, 14, 595
Curiel, S., Rodriguez, L. F., Bohigas, J., et al. 1989, ApL&C, 27, 299
Downes, D., & Rinehart, R. 1966, ApJ, 144, 937
Guzmán, A. E., Garay, G., Rodríguez, L. F., et al. 2014, ApJ, 796, 117
Guzmán, A. E., Garay, G., Rodríguez, L. F., et al. 2016, ApJ, 826, 208
Hambly, N. C., Collins, R. S., Cross, N. J., et al. 2008, MNRAS, 384, 637
Harris, S. 1973, MNRAS, 162, 5
Hernández-Hernández, V., Zapata, L., Kurtz, S., & Garay, G. 2014, ApJ, 786, 38
Hewett, P. C., Warren, S. J., Leggett, S. K., & Hodgkin, S. T. 2006, MNRAS, 367, 454
Hoare, M. G., Purcell, C. R., Churchwell, E. B., et al. 2012, PASP, 124 939
Hodgkin, S. T., Irwin, M. J., Hewett, P. C., & Warren, S. J. 2009, MNRAS, 394, 675
Hofner, P., Cesaroni, R., Olmi, L., et al. 2007, A&A, 465, 197
Hofner, P., & Churchwell, E. 1996, A&AS, 120, 283
Inayoshi, K., Hosokawa, T., & Omukai, K. 2013, MNRAS, 431, 3036
Irwin, P. G. J., Teanby, N. A., & Davis, G. R. 2009, Icar, 203, 287
Johnston, K. G., Shepherd, D. S., Robitaille, T. P., & Wood, K. 2013, A&A, 551, 43
Kurtz, S., Churchwell, E., & Wood, D. O. S. 1994, ApJS, 91, 659
Kurtz, S., Hofner, P., & Vargas Álvarez, C. 2004, ApJS, 155, 149
Lampton, M., Margon, B., & Bowyer, S. 1976, ApJ, 208, 177
Lawrence, A., Warren, S. J., Almaini, O., et al. 2007, MNRAS, 379, 1599
Leurini, S., Codella, C., Zapata, L., et al. 2011, A&A, 530, A12
Mehringer, D. 1995, ApJ, 454, 782
Mezger, P., Zylka, R., & Wink, J. E. 1990, A&A, 228, 95
Molinari, S., Brand, J., Cesaroni, R., & Palla, F. 1996, A&A, 308, 573
Nomura, H., & Millar, T. J. 2004, A&A, 414, 409
Olmi, L., Cesaroni, R., Nero, R., & Walmsley, C. M. 1996, A&A, 315, 565
Palau, A., Walsh, C., Sánchez-Monge, Á., et al. 2017, MNRAS, 467, 2723
Panagia, N., & Felli, M. 1975, A&A, 39, 1
Reynolds, S. P. 1986, ApJ, 304, 713
Rodriguez, L. F., Moran, J. M., Franco-Hernández, R., et al. 2008, AJ, 135, 2370
Rosero, V., Hofner, P., Claussen, M., et al. 2016, ApJS, 227, 25
Rosero, V., Hofner, P., Kurtz, S., Bieging, J., & Araya, E. 2013, ApJS, 207, 12

Rosero, V., Hofner, P., McCoy, M., et al. 2014, ApJ, 796, 130
Sault, R. J., Teuben, P. J., & Wright, M. C. H. 1995, in ASP Conf. Ser. 77, Astronomical Data Analysis Software and Systems IV, ed. R. A. Shaw, H. E. Payne, & J. J. E. Hayes (San Francisco, CA: ASP), 433
Sridharan, T. K., Beuther, H., Schilke, P., Menten, K. M., & Wyrowski, F. 2002, ApJ, 566, 931
Urquhart, J. S., Hoare, M. G., Purcell, C. R., et al. 2009, A&A, 501, 539
van der Walt, D. J. 2014, A&A, 562, 68
Wood, D. O. S., & Churchwell, E. 1989, ApJS, 69, 831
Xie, T., Mundy, L. G., Vogel, S. N., & Hofner, P. 1996, ApJL, 473, L131
Zhang, Q., Hunter, T. R., Brand, J., et al. 2001, ApJ, 552, 167
Zhang, Q., Sridharan, T. K., Hunter, T. R., et al. 2007, A&A, 470, 269